# Flexible Mode Modelling of the InSight Lander and Consequences for the SEIS Instrument

**N. Murdoch[1] · D. Alazard[1] · B. Knapmeyer-Endrun[2] · N.A. Teanby[3] · R. Myhill[3]**

**Abstract** We present an updated model for estimating the lander mechanical noise on the InSight seismometer SEIS, taking into account the flexible modes of the InSight lander. This new flexible mode model uses the Satellite Dynamics Toolbox to compute the direct and the inverse dynamic model of a satellite composed of a main body fitted with one or several dynamic appendages. Through a detailed study of the sensitivity of our results to key environment parameters we find that the frequencies of the six dominant lander resonant modes increase logarithmically with increasing ground stiffness. On the other hand, the wind strength and the incoming wind angle modify only the signal amplitude but not the frequencies of the resonances. For the baseline parameters chosen for this study, the lander mechanical noise on the SEIS instrument is not expected to exceed the instrument total noise requirements. However, in the case that the lander mechanical noise is observable in the seismic data acquired by SEIS, this may provide a complementary method for studying the ground and wind properties on Mars.

**Keywords** Mars · Seismology · Atmosphere · Regolith · Geophysics · Structural dynamics

## 1 Introduction

The InSight mission, selected under the NASA Discovery program for launch in 2018, will perform the first comprehensive surface-based geophysical investigation of Mars. The InSight mission will use the SEIS (Seismic Experiment for Internal Structures) instrument to

✉ N. Murdoch
naomi.murdoch@isae.fr

1 Institut Supérieur de l'Aéronautique et de l'Espace (ISAE-SUPAERO), Université de Toulouse, 31055 Toulouse Cedex 4, France

2 Department of Planets and Comets, Max Planck Institute for Solar System Research, Gottingen, Germany

3 School of Earth Sciences, University of Bristol, Bristol, UK

advance our understanding of the formation and evolution of terrestrial planets and determine the current level of tectonic activity and impact flux on Mars. SEIS consists of two independent, 3-axis seismometers: an ultra-sensitive very broad band (VBB) seismometer; and a miniature, short-period (SP) seismometer that provides partial measurement redundancy and extends the high-frequency measurement capability (Lognonné and Pike 2015).

The seismometers and their respective signal preamplifier stages are mounted on the precision levelling structure (LVL) and, after arrival on Mars, they will be deployed on to the ground as an integrated package using a robotic arm. The seismometers are then isolated from the Martian weather by a Wind and Thermal Shield (WTS). In order for InSight to achieve the mission objectives, it is vitally important that the performance requirements of the SEIS instrument are met. However, there are many potential sources of noise on seismic instruments. In addition to the instrument self-noise, there are also environment parameters that are expected to impact the measurements. Adding to the complexity of the problem, the different environment on Mars, and the different deployment configuration (directly on the surface rather in a seismic vault, for example), compared to the Earth will result in different noise conditions for the Martian seismometer. Some examples of environmental noise contributions are the thermal and magnetic noise induced by temperature and magnetic field fluctuations (Mimoun et al. 2017), the ground deformation induced by the atmospheric pressure variations (Murdoch et al. 2017b), the dynamic pressure due to the wind acting directly on the seismometer (Lognonné et al. 1996), and ground tilt or ground motion due to the interaction of the wind shield or the lander and the Martian winds (Nishikawa et al. 2014; Lorenz 2012).

The latter has been studied in detail by Murdoch et al. (2017a), who make use of an elastic ground deformation model to evaluate the mechanical noise contributions on the SEIS instrument due to the interaction between the Martian winds and the InSight lander. They find that the lander mechanical noise may be a detectable signal on the InSight seismometers but, for the baseline SEIS deployment position, this noise is not expected to endanger the InSight mission objectives. However, Murdoch et al. (2017a) concentrate on the very broad band seismometer bandwidth: [0.01–1 Hz]. As such, they consider the lander, deck and legs, as an inelastic structure in the frequency band of interest, and do not include a detailed simulation of the lander resonances. However, the lander resonances may significantly increase the mechanical noise at higher frequencies and, therefore, could also impact the short-period seismometer. In addition to being potentially of interest for the noise estimations, the mechanical noise generated by the lander resonances may actually provide an additional seismic source for determining the seismic properties of the Martian subsurface.

In this paper we present an updated model for the mechanical noise simulations taking into account the flexible modes of the InSight lander. We then examine the seismic signal that will be produced on the InSight seismometers before studying in detail the sensitivity of our results to key environment parameters.

## 2 Flexible Mode Modelling of the InSight Lander

### 2.1 Nomenclature

The following notations will be used throughout this section (see also Fig. 1).

| | |
|---|---|
| $\mathcal{B}$ | Lander main body. |
| $\mathcal{A}_l$ | Left solar panel. |
| $\mathcal{A}_r$ | Right solar panel. |
| $\mathcal{G}$ | Ground. |
| $\mathcal{R} = (O, \mathbf{x}, \mathbf{y}, \mathbf{z})$ | Lander main body ($\mathcal{B}$) reference frame. |
| $G$ | Lander main body ($\mathcal{B}$) centre of mass. |
| $G_i$ | Appendage's ($\mathcal{A}_i$) centre of mass ($i = r, l$). |
| $G_t$ | Overall lander centre of mass. |
| $P_i$ | Connection point of the appendage $\mathcal{A}_i$ on the main body $\mathcal{B}$ |
| $F_1$, $F_2$, $F_3$ | The 3 feet of the main body $\mathcal{B}$. |
| $C_p$ | Center of pressure of aerodynamic loads. |
| $\mathbf{a}_G$ | Inertial acceleration (vector) of body $\mathcal{B}$ at point $G$. |
| $\dot{\boldsymbol{\omega}}$ | Angular acceleration (vector) of $\mathcal{R}$ with respect to the inertial frame. |
| $\mathbf{F}_{ext}$ | Resultant external forces (vector) applied to $\mathcal{B}$. |
| $\mathbf{T}_{ext,G}$ | Resultant external torques (vector) applied to $\mathcal{B}$ at point $G$. |
| $\mathbf{F}_{\mathcal{G}/\mathcal{B},k}$ | Force (vector) applied by ground $\mathcal{G}$ on body $\mathcal{B}$ at foot $k$ ($k = 1, 2, 3$). |
| $\mathbf{F}_{w/\mathcal{B}}$ | Aerodynamic force (vector) applied on body $\mathcal{B}$ at $C_p$. |
| $\mathbf{F}_{\mathcal{B}/\mathcal{A}_i}$ | Internal force (vector) applied by $\mathcal{B}$ on $\mathcal{A}_i$. |
| $\mathbf{T}_{\mathcal{B}/\mathcal{A}_i,P_i}$ | Torque (vector) applied by $\mathcal{B}$ on $\mathcal{A}$ at point $P_i$. |
| $\boldsymbol{\tau}_{AB}$ | $6 \times 6$ kinematic model between points $A$ and $B$ $\boldsymbol{\tau}_{AB} = \left[\begin{smallmatrix} \mathbf{1}_3 & [^*\overrightarrow{AB}] \\ \mathbf{0}_{3\times3} & \mathbf{1}_3 \end{smallmatrix}\right]$. |
| $[^*\overrightarrow{AB}]$ | $3 \times 3$ skew anti-symmetric matrix associated with vector $\overrightarrow{AB}$ $[^*\overrightarrow{AB}] = \left[\begin{smallmatrix} 0 & -z & y \\ z & 0 & -x \\ -y & x & 0 \end{smallmatrix}\right]$ for $\overrightarrow{AB} = \left[\begin{smallmatrix} x \\ y \\ z \end{smallmatrix}\right]$. |
| $m^{\mathcal{X}}$ | Mass of body $\mathcal{X}$, ($\mathcal{X} = \mathcal{B}, \mathcal{A}_l, \mathcal{A}_r$). |
| $\mathbb{I}_P^{\mathcal{X}}$ | $3 \times 3$ inertia tensor of body $\mathcal{X}$ at point $P$. |
| $n^{\mathcal{X}}$ | Number of flexible modes in body $\mathcal{X}$. |
| $\boldsymbol{\eta}^{\mathcal{X}}$ | Modal coordinates vector for body $\mathcal{X}$. |
| $\omega_j^{\mathcal{X}}$ | $j$th flexible mode frequency for body $\mathcal{X}$. |
| $\xi$ | Flexible mode common damping ratio ($\xi = 0.005$). |
| $\mathbf{l}_{j,P}^{\mathcal{X}}$ | $1 \times 6$ vector of modal participation factors of the $j$th flexible mode of body $\mathcal{X}$, expressed at point $P$. |
| $\mathbf{L}_P^{\mathcal{X}}$ | $n \times 6$ matrix of the modal participation factors for body $\mathcal{X}$ expressed at point $P$: ($\mathbf{L}_P^{\mathcal{X}} = [\mathbf{l}_{1,P}^{\mathcal{X}^T}, \mathbf{l}_{2,P}^{\mathcal{X}^T}, \ldots, \mathbf{l}_{n^{\mathcal{X}},P}^{\mathcal{X}^T}]^T$). |
| s | LAPLACE variable. |

## 2.2 Satellite Dynamics Toolbox (SDT) Summary

The objective of the Satellite Dynamics Toolbox (Alazard and Cumer 2014) is to compute the direct and the inverse dynamic model of a satellite composed a main body $\mathcal{B}$ fitted with one or several dynamic appendages $\mathcal{A}_i$ cantilevered or hinged to the main body at point $P_i$. Each appendage is considered as a dynamic sub-structure either because of its flexibility or because of an embedded angular momentum (reaction wheels or control moment gyros) or liquid sloshing. For the InSight lander only cantilevered flexible appendages (the left and right solar panels) are considered.

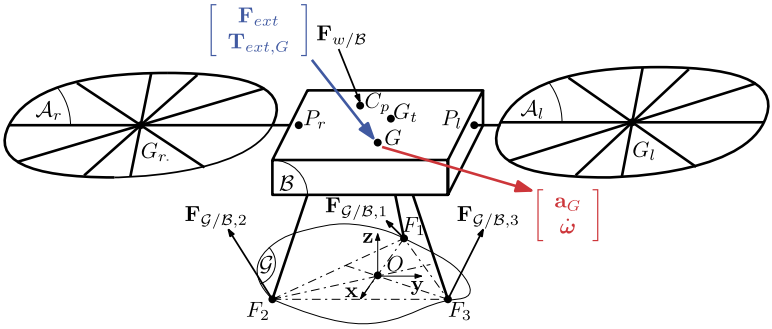


**Fig. 1** Simplified sketch of the InSight lander

The direct dynamic model $\mathbf{D}_G^{\mathcal{B}+\Sigma\mathcal{A}_i}(\mathrm{s})$ stands for the $6\times 6$ linear transfer between the acceleration twist (time-derivative of the twist) $\begin{bmatrix}\mathbf{a}_G\\ \dot{\boldsymbol{\omega}}\end{bmatrix}$ of the hub seen at its centre of mass $G$ (on input) and the wrench of the external forces and torques $\begin{bmatrix}\mathbf{F}_{ext}\\ \mathbf{T}_{ext,G}\end{bmatrix}$ applied to the hub at point $G$ (on output):

$$\begin{bmatrix}\mathbf{F}_{ext}\\ \mathbf{T}_{ext,G}\end{bmatrix} = \mathbf{D}_G^{\mathcal{B}+\Sigma\mathcal{A}_i}(\mathrm{s})\begin{bmatrix}\mathbf{a}_G\\ \dot{\boldsymbol{\omega}}\end{bmatrix}.$$

This linear model is only valid for small variations around the equilibrium conditions and requires the following assumptions:

(H1) The main body is rigid: $\frac{d\overrightarrow{GP_i}}{dt}|_{\mathcal{R}} = 0,\ \forall i$. For the main body of the InSight lander, it is thus assumed that the feet are also rigid: $\frac{d\overrightarrow{GF_k}}{dt}|_{\mathcal{R}} = 0,\ \forall k$.
(H2) Non-linear terms (in $\boldsymbol{\omega}\wedge X_{3\times 3}\boldsymbol{\omega}$) of second or higher order are disregarded.
(H3) The only force (resp. torque) applied to the appendage $\mathcal{A}_i$ is the force $\mathbf{F}_{\mathcal{B}/\mathcal{A}_i}$ (resp. torque $\mathbf{T}_{\mathcal{B}/\mathcal{A}_i,P_i}$) applied by the main body $\mathcal{B}$ at the appendage connection point $P_i$.

Then the whole direct dynamic model $\mathbf{D}_G^{\mathcal{B}+\Sigma\mathcal{A}_i}(\mathrm{s})$ is the sum of the dynamic model of each substructure expressed at the point $G$ using the kinematic models $\boldsymbol{\tau}_{P_iG}$ (see nomenclature in Sect. 2.1):

$$\mathbf{D}_G^{\mathcal{B}+\Sigma\mathcal{A}_i}(\mathrm{s}) = \mathbf{D}_G^{\mathcal{B}} + \sum_i \boldsymbol{\tau}_{P_iG}^T \mathbf{D}_{P_i}^{\mathcal{A}_i}(\mathrm{s})\boldsymbol{\tau}_{P_iG} \tag{1}$$

where:

– $\mathbf{D}_G^{\mathcal{B}} = \begin{bmatrix} m^{\mathcal{B}}\mathbf{1}_3 & \mathbf{0}_{3\times 3}\\ \mathbf{0}_{3\times 3} & \mathbb{I}_G^{\mathcal{B}}\end{bmatrix}$ is the direct dynamic model of the main body $\mathcal{B}$ at its centre of mass $G$,
– $\mathbf{D}_{P_i}^{\mathcal{A}_i}(\mathrm{s})$ is the direct dynamic model of the appendage $\mathcal{A}_i$ at the connection point $P_i$ and can be represented by the block-diagram depicted in Fig. 2. The flexible mode data ($\omega_j^{\mathcal{A}_i}$, $\xi$, $\mathbf{L}_{P_i}^{\mathcal{A}_i}$) involved in this representation can be directly read from the modal analysis output file provided by the finite element software used to model the appendage $\mathcal{A}_i$ under the "clamped at point $P_i$" boundary condition.

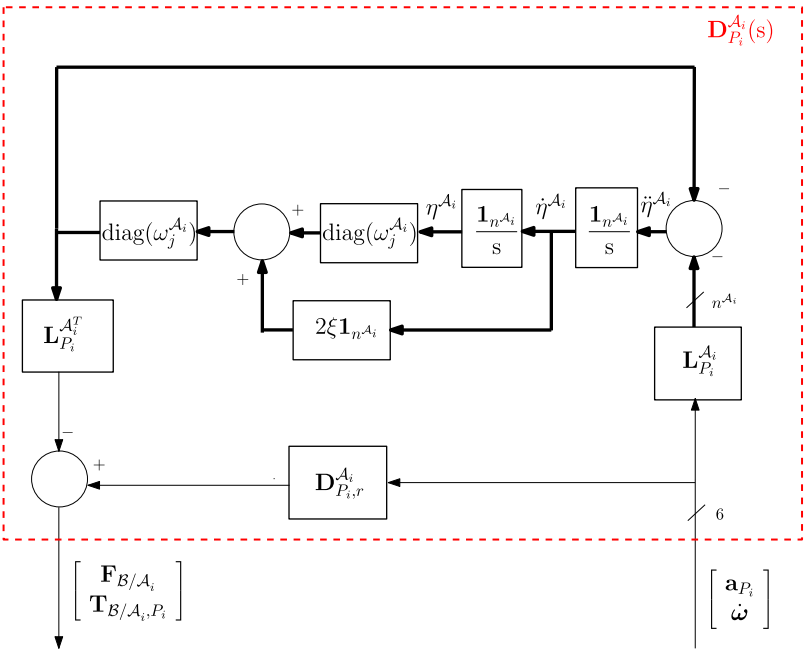


**Fig. 2** Block diagram representation of the direct dynamic model $\mathbf{D}_{P_i}^{\mathcal{A}_i}(\mathrm{s})$ of the flexible appendage $\mathcal{A}_i$ written at point $P_i$

Finally, $\mathbf{D}_{P_i,r}^{\mathcal{A}_i}$ is the $6\times 6$ residual mass matrix at the point $P_i$:

$$\mathbf{D}_{P_i,r}^{\mathcal{A}_i} = \underbrace{\boldsymbol{\tau}_{G_i P_i}^T \underbrace{\begin{bmatrix} m^{\mathcal{A}_i}\mathbf{1}_3 & \mathbf{0}_{3\times 3} \\ \mathbf{0}_{3\times 3} & \mathbb{I}_{G_i}^{\mathcal{A}_i}\end{bmatrix}}_{\mathbf{D}_{G_i}^{\mathcal{A}_i}(0)} \boldsymbol{\tau}_{G_i P_i}}_{\mathbf{D}_{P_i}^{\mathcal{A}_i}(0)} - \mathbf{L}_{P_i}^{\mathcal{A}_i T}\mathbf{L}_{P_i}^{\mathcal{A}_i},$$

i.e. the total mass of appendage $\mathcal{A}_i$ at point $P_i$ (the DC-gain of $\mathbf{D}_{P_i}^{\mathcal{A}_i}(\mathrm{s})$) minus the sum of modal participation factors squared.

The overall model can then be written at the global center of mass $G_t$ computed by the SDT:

$$\mathbf{D}_{G_t}^{\mathcal{B}+\Sigma\mathcal{A}_i}(\mathrm{s}) = \boldsymbol{\tau}_{GG_t}^T \mathbf{D}_{G}^{\mathcal{B}+\Sigma\mathcal{A}_i}(\mathrm{s})\boldsymbol{\tau}_{GG_t}.$$

The inverse overall model $[\mathbf{D}_{G}^{\mathcal{B}+\Sigma\mathcal{A}_i}]^{-1}(\mathrm{s})$, commonly used for control design and performances analyses, can be written as:

$$\left[\mathbf{D}_{G}^{\mathcal{B}+\Sigma\mathcal{A}_i}\right]^{-1}(\mathrm{s}) = \left[\mathbf{D}_{G}^{\mathcal{B}}\right]^{-1}\left(\mathbf{1}_6 + \left(\sum_i \boldsymbol{\tau}_{P_i G}^T \mathbf{D}_{P_i}^{\mathcal{A}_i}(\mathrm{s})\boldsymbol{\tau}_{P_i G}\right)\left[\mathbf{D}_{G}^{\mathcal{B}}\right]^{-1}\right)^{-1}. \tag{2}$$

This expression highlights that the direct dynamic model of each appendage $\mathcal{A}_i$ acts in feedback loop on the inverse dynamic model of the main body $\mathcal{B}$. In the case of a single appendage, this loop operation is depicted in Fig. 3.

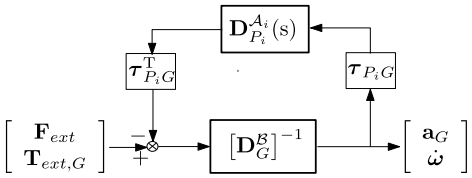


**Fig. 3** Inverse dynamics model $[\mathbf{D}_G^{\mathcal{B}+\mathcal{A}_i}]^{-1}(\mathrm{s})$ of the main body $\mathcal{B}$ and its appendage $\mathcal{A}_i$

This block-diagram representation of the dynamic model of the overall spacecraft is very convenient for several reasons:

- it does not require the inversion of the high order model $\mathbf{D}_{P_i}^{\mathcal{A}_i}(\mathrm{s})$ which includes various flexible modes,
- it is compliant with the various sub-structures of the spacecraft in that sense that each dynamic parameter of each sub-structure (mass, inertia, flexible mode frequency, ...) can be very easily isolated and appears with a minimal occurrence. Thus, it is particularly efficient for parametric sensitivity analyses (Guy et al. 2014).

## 2.3 Application to the InSight Lander

The SDT can be directly applied to the Insight lander, composed of the main body $\mathcal{B}$, the left $\mathcal{A}_l$ and the right $\mathcal{A}_r$ solar panels, to obtain the inverse dynamic model denoted:

$$\begin{aligned}\left[\mathbf{D}_G^{\mathcal{IS}}\right]^{-1}(\mathrm{s}) &= \left[\mathbf{D}_G^{\mathcal{B}+\mathcal{A}_l+\mathcal{A}_r}\right]^{-1}(\mathrm{s})\\ &= \left[\mathbf{D}_G^{\mathcal{B}}\right]^{-1}\left(\mathbf{1}_6+\left(\boldsymbol{\tau}_{P_lG}^T\mathbf{D}_{P_l}^{\mathcal{A}_l}(\mathrm{s})\boldsymbol{\tau}_{P_lG}+\boldsymbol{\tau}_{P_rG}^T\mathbf{D}_{P_r}^{\mathcal{A}_r}(\mathrm{s})\boldsymbol{\tau}_{P_rG}\right)\left[\mathbf{D}_G^{\mathcal{B}}\right]^{-1}\right)^{-1},\end{aligned}$$

such that:

$$\begin{bmatrix}\mathbf{a}_G\\ \dot{\boldsymbol{\omega}}\end{bmatrix} = \left[\mathbf{D}_G^{\mathcal{IS}}\right]^{-1}(\mathrm{s})\begin{bmatrix}\mathbf{F}_{ext}\\ \mathbf{T}_{ext,G}\end{bmatrix}. \tag{3}$$

The resultant wrench $\begin{bmatrix}\mathbf{F}_{ext}\\ \mathbf{T}_{ext,G}\end{bmatrix}$ is the sum of several interactions with the lander environment.

### *2.3.1 Interaction with the Martian Ground $\mathcal{G}$*

From the double integration of the acceleration twist $\begin{bmatrix}\mathbf{a}_G\\ \dot{\boldsymbol{\omega}}\end{bmatrix}$, one can deduce the position variations of the point $G$ along the 6 degrees of freedom $(\delta x_G, \delta y_G, \delta z_G, \delta\varphi, \delta\theta, \delta\psi)$ and their time-derivatives $(\dot{\delta x}_G, \dot{\delta y}_G, \dot{\delta z}_G, \dot{\delta\varphi}, \dot{\delta\theta}, \dot{\delta\psi})$. The position variations and rates of each foot $k$ $(k = 1, 2, 3)$ can then be determined using the kinematic model $\boldsymbol{\tau}_{F_kG}$:

$$\begin{bmatrix}\delta x_k\\ \delta y_k\\ \delta z_k\\ \delta\varphi\\ \delta\theta\\ \delta\psi\end{bmatrix} = \boldsymbol{\tau}_{F_kG}\begin{bmatrix}\delta x_G\\ \delta y_G\\ \delta z_G\\ \delta\varphi\\ \delta\theta\\ \delta\psi\end{bmatrix} \quad \text{and} \quad \begin{bmatrix}\dot{\delta x}_k\\ \dot{\delta y}_k\\ \dot{\delta z}_k\\ \dot{\delta\varphi}\\ \dot{\delta\theta}\\ \dot{\delta\psi}\end{bmatrix} = \boldsymbol{\tau}_{F_kG}\begin{bmatrix}\dot{\delta x}_G\\ \dot{\delta y}_G\\ \dot{\delta z}_G\\ \dot{\delta\varphi}\\ \dot{\delta\theta}\\ \dot{\delta\psi}\end{bmatrix}.$$

It is then assumed that no torque can be transmitted in the foot junction between the ground and the main body, only an interaction force which is proportional to the position variations through the isotropic ground stiffness matrix $\mathbf{K}_{\mathcal{G}}$ and proportional to the variations rates

through the isotropic ground damping matrix $\mathbf{D}_{\mathcal{G}}$ (see Sect. 3.1 for an explanation of these ground parameters):

$$\mathbf{F}_{\mathcal{G}/\mathcal{B},k} = -\mathbf{D}_{\mathcal{G}} \begin{bmatrix} \dot{\delta x}_k \\ \dot{\delta y}_k \\ \dot{\delta z}_k \end{bmatrix} - \mathbf{K}_{\mathcal{G}} \begin{bmatrix} \delta x_k \\ \delta y_k \\ \delta z_k \end{bmatrix}, \quad \forall\, k = 1, 2, 3, \text{ with the baseline assumptions of:}$$

$$\mathbf{K}_{\mathcal{G}} = \begin{bmatrix} K_s & 0 & 0 \\ 0 & K_s & 0 \\ 0 & 0 & K_s \end{bmatrix} \left(10^6\,\mathrm{N/m}\right), \ \mathbf{D}_{\mathcal{G}} = \begin{bmatrix} D & 0 & 0 \\ 0 & D & 0 \\ 0 & 0 & D \end{bmatrix} \text{(kg/s)}.$$

### 2.3.2 *Interaction with the Martian Wind*

As in Murdoch et al. (2017a), the aerodynamic load is characterized by a force $\mathbf{F}_{w/\mathcal{B}}$ applied to the center of pressure $C_p$ of the whole lander and reads:

$$\mathbf{F}_{w/\mathcal{B}} = \begin{bmatrix} \frac{1}{2}\rho v^2 \lambda S C_d \sin\beta \\ \frac{1}{2}\rho v^2 \lambda S C_d \cos\beta \\ \frac{1}{2}\rho v^2 \lambda S C_l \end{bmatrix} = \begin{bmatrix} k_x \\ k_y \\ k_z \end{bmatrix} v^2 \quad \text{with: } \lambda = \frac{\ln^2(z/z_0)}{\ln^2(z_r/z_0)}$$

and where:

- $\rho = 0.0155$ kg/m$^3$: day time air density,
- $z_0 = 0.01$ m: surface roughness length,
- $z_r = 1.61$ m: wind reference height (see Murdoch et al. 2017a),
- $z = 1.07$ m: the height of the solar panels above the surface, $\mathcal{G}$ (Murdoch et al. 2017a),
- $S = 7.53$ m$^2$: surface exposed to the lift and drag force (Murdoch et al. 2017a),
- $C_d$: drag coefficient of the lander varies as a function of the vertical angle of attack (Fig. 4),
- $C_l$: lift coefficient of the lander varies as a function of the vertical angle of attack (Fig. 4),
- $\beta$ (rad): direction of the wind in the horizontal $(O, \mathbf{x}, \mathbf{y})$ plane,
- $\alpha$ (rad): direction of the wind in the vertical $(O, \mathbf{x}, \mathbf{z})$ plane,
- $v$ (m/s) is the random wind velocity,
- $K_s$: the ground stiffness under the lander feet (see Sect. 3.1),
- $D$: the damping of the ground under the lander feet (see Sect. 3.1).

$w = v^2$ is considered as the input of the mechanical noise model and is defined by its Amplitude Spectral Density (expressed in m$^2$/s$^2$/$\sqrt{(}$Hz); Murdoch et al. 2017a).

Finally the center of pressure $C_p$ depends also on $\beta$ (see Murdoch et al. 2017a):

$$\overrightarrow{OC_p} = \begin{bmatrix} -(l_0/4)\cos\beta + x_0 \\ -(l_0/4)\sin\beta \\ h_0 \end{bmatrix}_{\mathcal{R}}$$

with:

- $l_0 = 2.218$ m: solar panel chord location,
- $x_0 = -0.49$ m: solar panel offset with respect to the geometric centre of the lander body,
- $h_0 = 0.777$ m: the height of the lander centre of gravity.

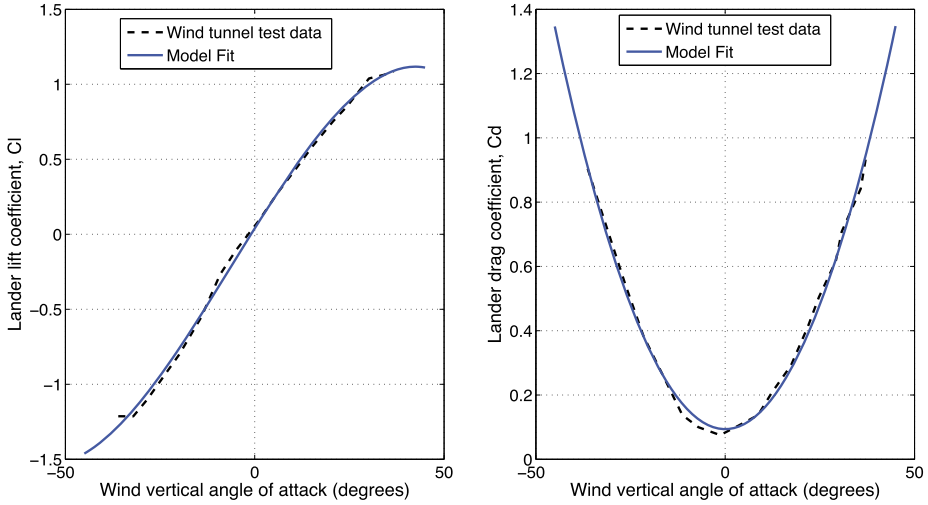


**Fig. 4** Lander lift and drag coefficients of the InSight lander as a function of vertical angle of attack ($\alpha$)—lander lift and drag coefficients as determine by wind tunnel tests are given by the dashed black line. As described in Murdoch et al. (2017a), we use a fit to this test data (shown by the solid blue line) to determine the lift and drag coefficients for our model

*Remark* Such a model is compliant with the assumption H3 but this assumption is restrictive to model the aerodynamic loads on the left and right solar panels independently and their coupling with the flexible modes of each solar panel.

### *2.3.3 Mechanical Noise Overall Model*

The 4 external forces $\mathbf{F}_{\mathcal{G}/\mathcal{B},k}$, $k = 1, 2, 3$ and $\mathbf{F}_{w/\mathcal{B}}$ can then be transported to the main body centre of mass $G$ using the kinematics models transposed to expressed the resultant wrench:

$$\begin{bmatrix} \mathbf{F}_{ext} \\ \mathbf{T}_{ext,G} \end{bmatrix} = \sum_{k=1}^{3} \boldsymbol{\tau}_{F_k G}^{T} \begin{bmatrix} \mathbf{F}_{\mathcal{G}/\mathcal{B},k} \\ \mathbf{0}_{3\times 1} \end{bmatrix} + \boldsymbol{\tau}_{C_p G}^{T} \begin{bmatrix} \mathbf{F}_{w/\mathcal{B}} \\ \mathbf{0}_{3\times 1} \end{bmatrix}.$$

Then, the full $9 \times 1$ model between the wind velocity squared $w = v^2$ (input) and the 3 force vectors transmitted by the ground to the 3 lander feet $[\mathbf{F}_{\mathcal{G}/\mathcal{B},1}^T, \mathbf{F}_{\mathcal{G}/\mathcal{B},2}^T, \mathbf{F}_{\mathcal{G}/\mathcal{B},3}^T]^T$ (output) can be described by the block-diagram of Fig. 5. This model will be denoted $\mathbf{T}_{w\to\mathcal{G}}(\mathrm{s})$.

## 2.4 Numerical Application and Frequency-Domain Analysis

The numerical values of the various mechanical parameters of the InSight lander are summarized in Table 1. Vectors and tensors are expressed in the frame $\mathcal{R} = (0, \mathbf{x}, \mathbf{y}, \mathbf{z})$ (see Fig. 1). These data, in addition to ground parameters defined in Sect. 2.3.1 and aerodynamic parameters defined in Sect. 2.3.2, allow the model $\mathbf{T}_{w\to\mathcal{G}}(\mathrm{s})$, between the wind input ($w$) and the 9 outputs of the 3 interaction forces ($\mathbf{F}_{\mathcal{G}/\mathcal{B},1}$,$\mathbf{F}_{\mathcal{G}/\mathcal{B},2}$, $\mathbf{F}_{\mathcal{G}/\mathcal{B},3}$) between the ground and the 3 lander feet, to be evaluated for a given wind direction $\beta$.

For $\beta = 45°$ and $\alpha = 0°$ the frequency-domain responses are depicted in Fig. 6 (magnitude BODE plots of each output) and in Fig. 7 (the transfer singular value). On these figures,

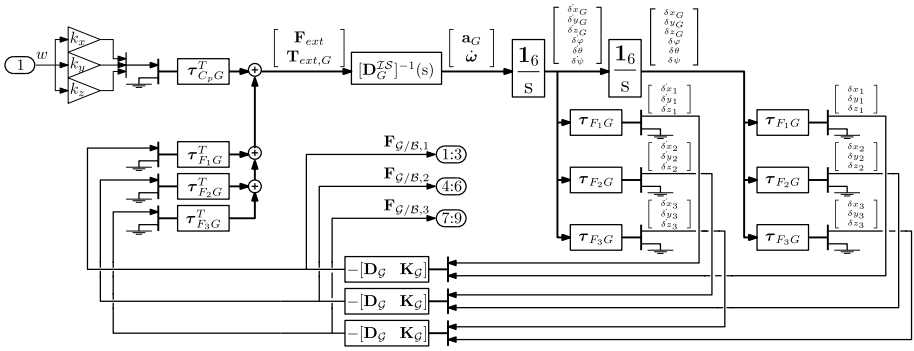

**Fig. 5** Block diagram representation of the mechanical noise model $\mathbf{T}_{w\to\mathcal{G}}(\mathrm{s})$

the responses obtained assuming the lander to be rigid are also plotted (dashed lines). The model assuming the lander is rigid is obtained just by changing the InSight lander model $[\mathbf{D}_g^{\mathcal{IS}}]^{-1}(\mathrm{s})$ by its DC-gain $[\mathbf{D}_g^{\mathcal{IS}}]^{-1}(0)$ in the whole model depicted in Fig. 5. The analysis of these responses leads to the following remarks:

- 6 high magnitudes resonances can be isolated in the frequency range between 100 and 600 rad/s. These resonances correspond to the 6 flexible modes associated to the 6 degrees of freedom spring-mass system composed of the lander mass and inertia clamped on the ground stiffness $\mathbf{K}_{\mathcal{G}}$. The dynamic coupling of these modes with the lander internal flexible modes (coming from the solar panels) are visible since one can notice the frequency shifts between the solid and the dashed plots (mainly in Fig. 7),
- the resonances coming from the solar panel flexible modes occur between 50 and 80 rad/s and have low magnitudes in comparison with the previous ones. Their contribution is most important on $z$ component of $\mathbf{F}_{\mathcal{G}/\mathcal{B},2}$ (Fig. 6, middle, bottom). Such a behaviour depends, of course, on the wind direction $\beta$.

These analyses demonstrate that the internal lander flexible mode modelling is required to have a good prediction of the main resonance frequencies in the overall lander mechanical model. The SDT is very convenient for that purpose. However, it should be noted that the assumption H3 is restrictive and that the magnitude of these internal modes may be significantly more important if the direct action of the wind on the solar panels was taken into account. To model the action of the wind on each solar panel, the projection of each flexible mode modal shape on the center of pressure is required (data not currently available). Then, complementary approaches developed in Gonzalez et al. (2016) and Chebbi et al. (2016) could be applied.

## 3 Baseline Parameter Assumptions

### 3.1 Ground Properties

The baseline ground properties (Table 2) are derived from the seismic velocities of Martian regolith simulant (Mojave sand), measured in laboratory tests (Morgan et al. 2018). As these values are for the regolith properties at the surface of Mars under an atmospheric pressure of 0.6 kPa, it is, therefore, necessary to extrapolate these values to the pressure found under the

**Table 1** InSight lander mechanical parameters assumed for this study

| Parameter | Numerical value | Unit |
|---|---|---|
| $\overrightarrow{OG}$ | $[-0.038,\ 0.001,\ 0.777]^T$ | m |
| $\overrightarrow{OP_l}$ | $[-0.492,\ 0.780,\ 1.07]^T$ | m |
| $\overrightarrow{OP_r}$ | $[-0.492;\ -0.780;\ 1.07]^T$ | m |
| $\overrightarrow{P_lG_l}$ | $[0,\ 1.109,\ 0]^T$ | m |
| $\overrightarrow{P_rG_r}$ | $[0,\ -1.109,\ 0]^T$ | m |
| $\overrightarrow{OF1}$ | $[-1.221,\ 0,\ 0]^T$ | m |
| $\overrightarrow{OF2}$ | $[0.610,\ -1.057,\ 0]^T$ | m |
| $\overrightarrow{OF3}$ | $[0.610,\ 1.057,\ 0]^T$ | m |
| $m^{\mathcal{B}}$ | 306.0 | kg |
| $\mathbb{I}_G^{\mathcal{B}}$ | $\begin{bmatrix} 94.122 & -0.175 & 2.959 \\ \star & 118.033 & -0.022 \\ \star & \star & 154.191 \end{bmatrix}$ | kg m$^2$ |
| $m^{\mathcal{A}_l} = m^{\mathcal{A}_r}$ | 29.2 | kg |
| $\mathbb{I}_{G_l}^{\mathcal{A}_l} = \mathbb{I}_{G_r}^{\mathcal{A}_r}$ | $\begin{bmatrix} 10.053 & 0.063 & 0.005 \\ \star & 5.738 & -0.659 \\ \star & \star & 15.500 \end{bmatrix}$ | kg m$^2$ |
| $n^{\mathcal{A}_l} = n^{\mathcal{A}_r}$ | 12 | – |
| $\omega_{1:12}^{\mathcal{A}_l} = \omega_{1:12}^{\mathcal{A}_r}$ | [10.23, 10.86, 13.39, 15.35, 19.83, 20.46, 28.29, 29.13, 41.23, 42.03, 44.12, 44.56] | rad/s |
| $\xi$ | 0.005 | – |
| $\mathbf{L}_{P_l}^{\mathcal{A}_l} = \mathbf{L}_{P_r}^{\mathcal{A}_r}$ | [0.7027, 0.0395, 0.0561, 0.0773, 0.7068, 1.6359;<br>0.7427, 0.0457, 0.0585, 0.0776, 0.7319, 1.6071;<br>0.0355, 0.0074, 0.0689, 0.1388, 0.4037, 0.0530;<br>0.0189, 0.0120, 0.0680, 0.1713, 0.4214, 0.0067;<br>0.0260, 0.1560, 0.2447, 1.6070, 0.1164, 0.1512;<br>0.0296, 0.0762, 0.6875, 0.6938, 0.2708, 0.0440;<br>0.0338, 0.2959, 0.0883, 1.2388, 0.0256, 0.0953;<br>0.0392, 0.0395, 1.0760, 0.1218, 0.4507, 0.0188;<br>0.0214, 0.0043, 0.0012, 0.0030, 0.0244, 0.0164;<br>0.0165, 0.0049, 0.0031, 0.0016, 0.0169, 0.0120;<br>0.0267, 0.0560, 0.0767, 0.0238, 0.0076, 0.0015;<br>0.0348, 0.0692, 0.0754, 0.0229, 0.0226, 0.0066] | $\sqrt{\text{kg}}$, $\sqrt{\text{kg}}$/m |

The parameters in the first section of Table 1 come from Murdoch et al. (2017a). The distribution of mass between the lander body and the solar panels, and the inertia tensors are estimated values. The flexible mode frequencies ($\omega_{1:12}^{\mathcal{A}_l}$, $\omega_{1:12}^{\mathcal{A}_r}$), and the modal participation factor for the lander solar panels ($\mathbf{L}_{P_l}^{\mathcal{A}_l} = \mathbf{L}_{P_r}^{\mathcal{A}_r}$) were provided by Lockheed Martin

lander feet. First, the expected pressure under each foot of the lander on Mars is calculated and, then an extrapolation of the seismic velocities is performed assuming a power law based on laboratory measurements (for details see Murdoch et al. 2017a; Delage et al. 2017; Morgan et al. 2018). Note that the predicted elastic ground properties at the InSight landing site have been updated since Murdoch et al. (2017a). In this paper we use the values provided in Morgan et al. (2018) as our baseline ground properties.

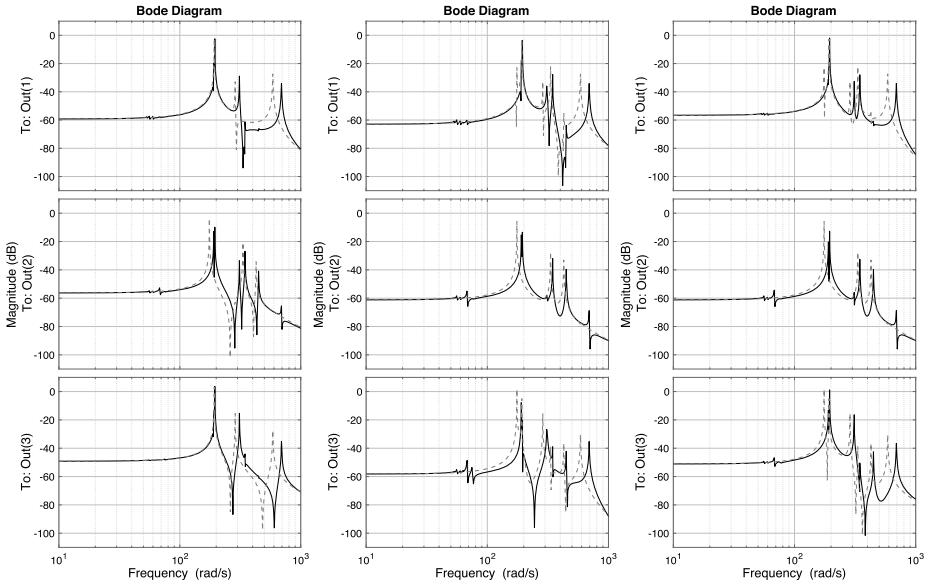


**Fig. 6** BODE magnitudes of transfer between $w$ and $\mathbf{F}_{\mathcal{G}/\mathcal{B},1}$ (left), $\mathbf{F}_{\mathcal{G}/\mathcal{B},2}$ (middle), $\mathbf{F}_{\mathcal{G}/\mathcal{B},3}$ (right)—full flexible model: solid black, rigid model: dashed gray. Here a ground stiffness of 10e6 N/m and a ground damping of 100 kg/s are assumed in order to demonstrate the various resonant modes

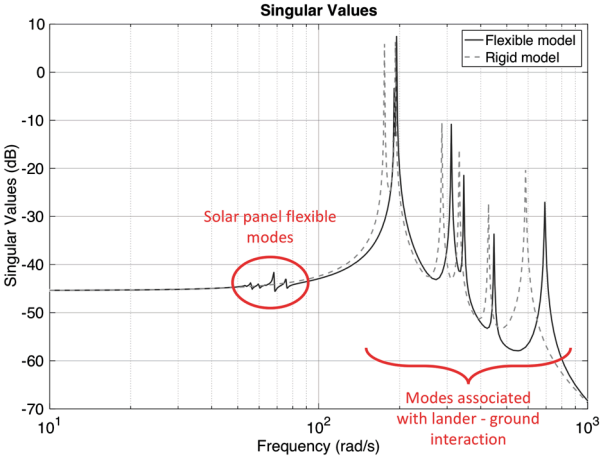


**Fig. 7** The singular value of the $9 \times 1$ transfer $\mathbf{T}_{w \to \mathcal{G}}(\mathrm{j}\omega)$—full flexible model: solid black, rigid model: dashed gray. The 6 resonant modes of the lander on the elastic ground are visible in both the rigid and non-rigid models but the flexible modes associated with the solar panels are only visible in the full flexible model. Here a ground stiffness of 10e6 N/m and a ground damping of 100 kg/s are assumed in order to demonstrate the various resonant modes

The Young's modulus ($E$), shear modulus ($\mu$) and Poisson ratio ($\nu$) can then be calculated using the regolith bulk density ($\rho_r$) and the $P$- and $S$-wave velocities ($v_P$, $v_S$):

$$E = \rho_r v_S^2 \frac{3v_P^2 - 4v_S^2}{v_P^2 - v_S^2} \tag{4}$$

$$\mu = \rho_r v_S^2 \tag{5}$$

$$\nu = \frac{v_P^2 - 2v_S^2}{2(v_P^2 - v_S^2)}. \tag{6}$$

**Table 2** Predicted Insight landing site surface regolith properties assuming an atmospheric pressure of 0.6 kPa and an averagely compact regolith (Morgan et al. 2018)

| | Bulk density, $\rho_r$ ($\mathrm{kg\,m^{-3}}$) | S-wave velocity, $v_S$ ($\mathrm{m\,s^{-1}}$) | P-wave velocity, $v_P$ ($\mathrm{m\,s^{-1}}$) | Confining pressure (kPa) |
|---|---|---|---|---|
| At the surface of Mars | ~1300 | 48.8 | 81.5 | 0.6 |
| Under the lander feet | ~1300 | 101.8 | 170.0 | 6.96 |
| Under the SEIS feet | ~1300 | 83.5 | 139.5 | 3.60 |
| At a depth of 1 m | 1307 | 94.6 | 157.9 | 5.44 |
| At a depth of 2 m | 1313 | 114.6 | 191.2 | 10.30 |

Using Hertzian mechanics the ground stiffness can be estimated. Assuming for simplicity that the lander feet are rigid and cylindrical in shape (radius of $r_f$), the indentation depth of the feet ($x$) for a given force ($F$) is given by:

$$x = \frac{F}{2 r_f E^*} \tag{7}$$

where $E^*$, a function of the Poisson's ratio and Young's modulus of the ground ($\nu$ and $E$, respectively) and of the lander feet ($\nu_f$ and $E_f$, respectively), is given by:

$$E^* = \frac{1}{\frac{1-\nu^2}{E} + \frac{1-\nu_f^2}{E_f}}. \tag{8}$$

The effective Young's modulus between the lander feet and the regolith is dominated by the Young's modulus of the regolith. The ground stiffness under the lander feet, $K_s$ (in N/m), can then be expressed as:

$$K_s = F/x = 2 r_f E^*. \tag{9}$$

According to Myhill et al. (2018), the damping of the ground under the lander feet, $D$ (in kg/s) for a given mass ($m$) can be expressed as:

$$D = 2\sqrt{K_s m} 0.05 = 0.1\sqrt{K_s \left(m^{\mathcal{B}} + m^{\mathcal{A}_l} + m^{\mathcal{A}_r}\right)}. \tag{10}$$

Based on the extrapolated seismic velocities at the surface of Mars, and assuming a lander foot radius of 14.4 cm and a total lander mass of 365 kg (Murdoch et al. 2017a), values of 9.93*e*6 N/m and 6020 kg/s are used as baseline ground parameters (underneath the InSight lander feet) in the isotropic ground stiffness matrix $\mathbf{K}_{\mathcal{G}}$ and the isotropic ground damping matrix $\mathbf{D}_{\mathcal{G}}$, respectively (as described in Sect. 2.3.1). However, as the coefficients in Eq. (10) are poorly constrained and the seismic velocities provided in Morgan et al. (2018) are simply informed estimates, the sensitivity of our results to both the ground stiffness and damping is studied in detail Sect. 5.1.

### 3.2 Wind Properties and Deployment Configuration

The baseline deployment configuration for SEIS, the wind and thermal shield (WTS) and the Heat Flow and Physical Properties Package (HP3, the second InSight instrument; Spohn

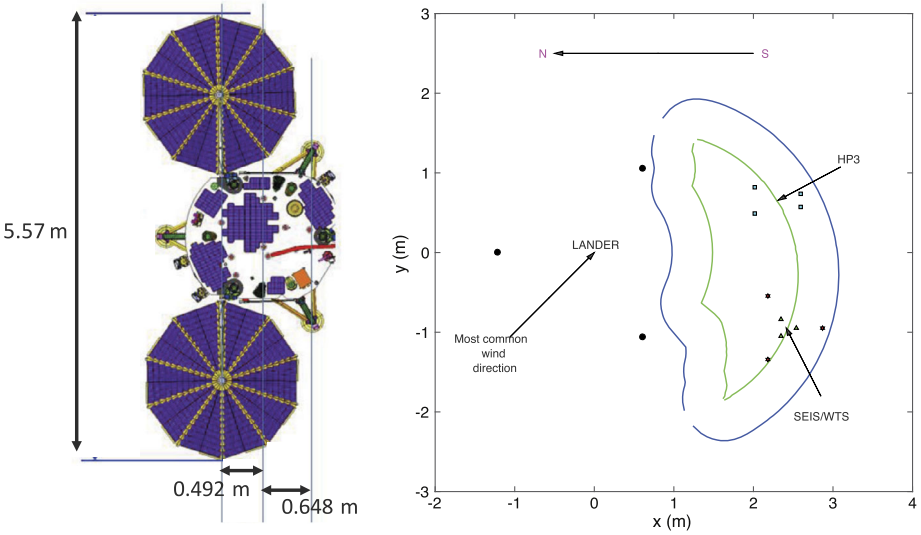


**Fig. 8** The InSight lander and baseline deployment configuration—(left) the lander dimensions are provided in the diagram. The solar panels are offset with respect to lander body by 49.2 cm. (Right) The three black circles indicate the locations of the three lander feet. The deployment zone is to the south of the lander. The blue and green lines shown the possible deployment zones for the WTS and SEIS, respectively. The baseline deployment locations of SEIS and the WTS are shown by the green triangles and red stars, and the baseline deployment location of HP3 is shown by the cyan squares. The figure is to scale. The dominant wind direction is expected to be from the North-West

et al. 2014) is given in Fig. 8. In this baseline configuration, it is anticipated that InSight will be aligned along the North-South axis with the deployment zone to the South (Fig. 8). As the average large-scale wind at the InSight landing site is expected to be from the North-West (Mars Climate Database version 5.2 Millour et al. 2015; Spiga et al. 2018; Golombek et al. 2018), we assume a wind from the North-West as the most common wind direction for this study. As a consequence, when the wind comes from the North, SEIS is downwind of the lander. For the baseline case, it is also assumed that the lander is not inclined and that the wind is parallel to the surface giving a vertical angle of attack of zero degrees.

In Murdoch et al. (2017a) linear models are provided for the predicted wind speed squared spectral amplitudes on Mars, based on previous in-situ data at low frequency and theoretical arguments at high frequency. These linear models give an estimation of the amplitude of the upper limits for the night and day spectral amplitude of the wind speed 50%, 70% and 95% of the time. As in Murdoch et al. (2017a), we assume that the baseline spectral amplitude is that of the upper limit for the day time data 70% of the time.

## 4 Seismic Signal on the InSight Seismometers

The force exerted on the ground at the three lander feet is calculated using the flexible mode modelling (Sect. 2), and the previously stated wind and ground property assumptions (Sect. 3). The resulting ground deformation at the base of the SEIS levelling structure, and thus the seismic signal on the seismometers is calculated using the same elastic ground deformation model as described in Murdoch et al. (2017a). That is to say that, we model the

ground as an elastic half-space with properties of a Martian regolith (this is possible given the small distances between lander and SEIS feet compared to the thickness of the regolith layer) and then use the Boussinesq point load solution (Boussinesq 1885) to determine the deformation of the elastic medium caused by forces applied to its free surface. Assume a point force $\mathbf{F} = F_1\mathbf{e_1} + F_2\mathbf{e_2} + F_3\mathbf{e_3}$ that is applied at the point $\boldsymbol{\xi} = \xi_1\mathbf{e_1} + \xi_2\mathbf{e_2} + \xi_3\mathbf{e_3}$ and $\boldsymbol{\Lambda} = \Lambda_1\mathbf{e_1} + \Lambda_2\mathbf{e_2} + \Lambda_3\mathbf{e_3}$ is some arbitrary point in the half-space $\Lambda_3 \geq 0$. The Green's tensor for displacements ($G_{ik}$), defined by the relation $u_i = \sum_k G_{ik}F_k$, may be written in Cartesian coordinates as (solution from Landau and Lifshitz 1970):

$$G_{ik} = \frac{1}{4\pi\mu}\begin{bmatrix} \frac{b}{r} + \frac{x^2}{r^3} - \frac{ax^2}{r(r+z)^2} - \frac{az}{r(r+z)} & \frac{xy}{r^3} - \frac{ayx}{r(r+z)^2} & \frac{xz}{r^3} - \frac{ax}{r(r+z)} \\ \frac{yx}{r^3} - \frac{ayx}{r(r+z)^2} & \frac{b}{r} + \frac{y^2}{r^3} - \frac{ay^2}{r(r+z)^2} - \frac{az}{r(r+z)} & \frac{yz}{r^3} - \frac{ay}{r(r+z)} \\ \frac{zx}{r^3} - \frac{ax}{r(r+z)} & \frac{zy}{r^3} - \frac{ay}{r(r+z)} & \frac{b}{r} + \frac{z^2}{r^3} \end{bmatrix}$$

where $x = \Lambda_1 - \xi_1$, $y = \Lambda_2 - \xi_2$, $z = \Lambda_3 - \xi_3$, and $r$ is the magnitude of the vector between $\boldsymbol{\Lambda}$ and $\boldsymbol{\xi}$, $a = (1 - 2\nu)$ and $b = 2(1 - \nu)$, $\nu$ is Poisson's ratio and $\mu$ is the shear modulus (as defined in Sect. 3.1). For our calculations, we assume that $\Lambda_3 = 0$ and $\xi_3 = 0$ i.e., the lander and SEIS feet are all on the surface of the regolith. The Green's tensor then simplifies to:

$$G_{ik} = \frac{1}{4\pi\mu}\begin{bmatrix} \frac{b}{r} + \frac{x^2}{r^3} - \frac{ax^2}{r^3} & \frac{xy}{r^3} - \frac{ayx}{r^3} & -\frac{ax}{r^2} \\ \frac{yx}{r^3} - \frac{ayx}{r^3} & \frac{b}{r} + \frac{y^2}{r^3} - \frac{ay^2}{r^3} & -\frac{ay}{r^2} \\ -\frac{ax}{r^2} & -\frac{ay}{r^2} & \frac{b}{r} \end{bmatrix}.$$

There are two components to the acceleration felt by SEIS: the acceleration from the direct motion of the ground (in the horizontal and vertical axes), and the acceleration due to different vertical displacements of the SEIS feet that causes an inclination of the seismometer in the gravity field (signal in the horizontal axes only). The former dominates at high frequencies, where as the tilt signal dominates at low frequencies.

The results of the original inelastic lander structure model (Murdoch et al. 2017a) and the new, flexible mode lander model, are shown in Fig. 9 for the baseline parameters provided in Sect. 2 and Sect. 3. The two models give identical results at low frequency but the lander resonances can clearly be seen at frequencies of ~10 Hz and above in the flexible mode model. As described in Sect. 2, the first modes (at ~10 Hz) are due to the flexible modes of the solar panels, and the higher magnitude and higher frequency resonances correspond to the 6 flexible modes associated with the 6 degrees of freedom interaction of the lander body and the Martian regolith (not all 6 modes are visible here due to the ground damping; see Sect. 5.1).

Note that the baseline parameters chosen for this study are slightly different to those used in Murdoch et al. (2017a). Specifically, we use the updated ground properties (as provided in Sect. 3) and we assume a that the vertical angle of attack of the wind with respect to the lander is zero degrees (rather than taking the estimated worst case of 15° as used in Murdoch et al. 2017a).

## 5 Parameter Sensitivity

### 5.1 Sensitivity to Ground Properties

Despite the efforts that have been made to constrain the properties of the InSight landing site regolith (Delage et al. 2017; Morgan et al. 2018), the regolith may have a large range of

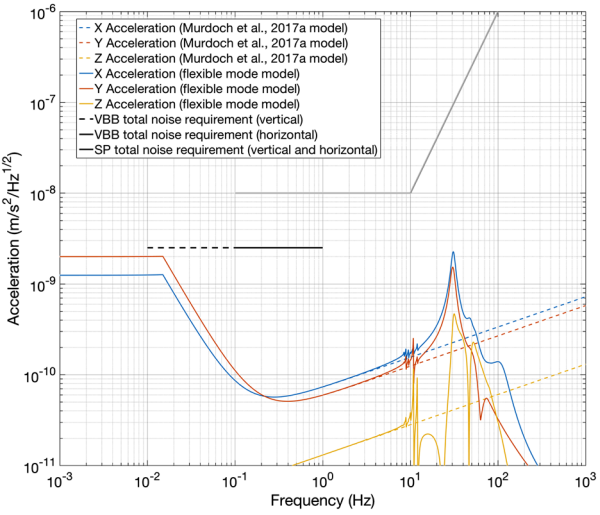


**Fig. 9** Model comparison—the lander mechanical noise signal on SEIS as calculated using the inelastic lander structure model of Murdoch et al. (2017a) (dashed coloured lines), and using the new lander flexible mode model presented here (solid coloured lines). The baseline parameters for this study, as presented in Sect. 2 and Sect. 3 were used. The total noise requirements for the seismic sensors are provided in black for the VBB sensors and grey for the SP sensors

elastic properties. Determination of these properties will be an important part of the InSight mission (Golombek et al. 2018). Here we examine the influence of the two most important ground properties for our flexible mode model: the ground stiffness and the ground damping.

Although these two parameters are related (see Sect. 3.1), we first consider them individually to understand their respective influences on the lander resonances. As the ground stiffness increases, the frequencies of the solar panel resonances (at ∼10 Hz) do not vary as they are dictated by the mechanics of the attachment point with the main lander. However, the lander body - ground resonances shift to higher frequency and their amplitude increases (Fig. 10, left). This is further highlighted in Fig. 11 showing the variation of resonant frequencies with ground stiffness: the frequencies of the six resonant modes (corresponding to the six degrees of freedom of the lander) increase logarithmically (slope $= 1/2$) with increasing ground stiffness. The resonances due to the solar panels (at ∼10 Hz; Fig. 10, left) are most evident when the ground stiffness is smallest due to the combined effect of the solar panel and lander-ground resonances in the same bandwidth. Note that we consider a large ground stiffness range for our analyses as the expected value of the Young's modulus for the Martian regolith is poorly constrained (Morgan et al. 2018).

This logarithmic dependence of the resonance frequencies on ground stiffness can be understood intuitively by considering the lander body and the Martian ground as two springs attached in series. As the 'lander body spring' ($K_{\mathcal{B}}$) is much stiffer than the 'Martian ground spring' ($K_s$) the effective spring constant of the system is dominated by the 'Martian ground spring':

$$\frac{1}{K_{eff}} = \frac{1}{K_{\mathcal{B}}} + \frac{1}{K_s} \sim \frac{1}{K_s}. \tag{11}$$

Then, as the natural frequency ($f_0$) of this simple mechanical system varies as:

$$f_0 \propto \sqrt{K_s}, \tag{12}$$

this leads to the $1/2$ logarithmic slope shown in Fig. 11 as the ground stiffness ($K_s$) increases.

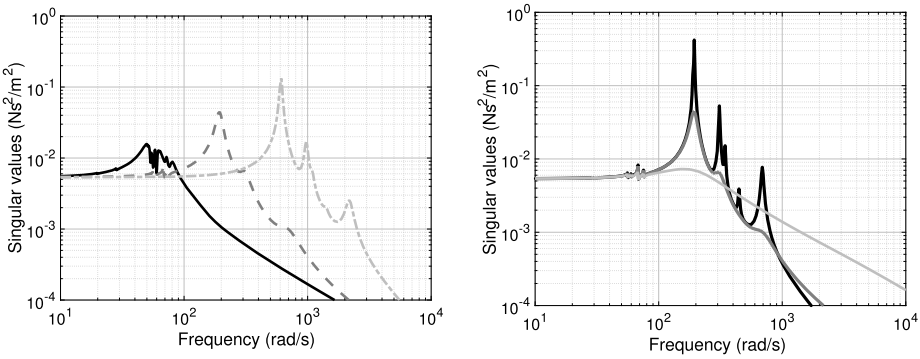


**Fig. 10** Variation of the resonant mode singular values with ground parameters—(left) variation of the resonant mode singular values with ground stiffness. Here the results of the baseline ground stiffness are shown (dark grey dashed line) as are the results for a ground stiffness ten times less than the baseline ground stiffness (solid black line) and ten times more than the baseline ground stiffness (dashed light grey line). To isolate the influence of the ground stiffness the ground damping is kept constant at the baseline value. (Right) Variation of the resonant mode singular values with ground damping. Here the results of the baseline ground damping are shown (dark grey line) as are the results for a ground damping ten times less than the baseline ground damping (black line) and ten times more than the baseline ground damping (light grey line). To isolate the influence of the ground damping the ground stiffness is kept constant at the baseline value

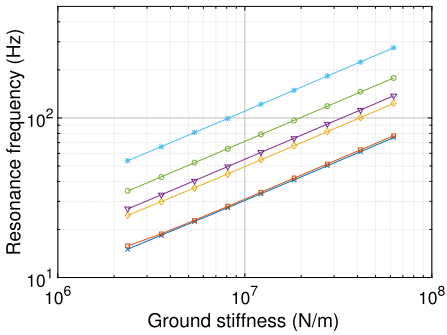


**Fig. 11** Variation of resonant frequencies with ground stiffness—each line corresponds to the peak frequency of the six different resonant modes. The frequencies of the six resonant modes (corresponding to the six degrees of freedom of the lander) increase logarithmically with increasing ground stiffness

The ground damping has no influence on the resonances due to the solar panels (at ∼10 Hz). However, there is a significant decrease in the amplitude of the resonances due to the lander body—ground interaction as the magnitude of the ground damping parameter increases (Fig. 10, right and Fig. 12). The damping does not influence the frequencies of any of the resonances.

The combined influence of these two ground parameters on the resulting forces applied on the ground by the lander each lander feet is shown in Fig. 13. The ground stiffness is varied and the ground damping parameter thus also varies according to the relation in Eq. (10). The consequence of the ground stiffness and associated ground damping variation on the resulting seismic signal measured by SEIS can then be seen in Fig. 14. Over the entire bandwidth, the amplitude of the seismic signal is much larger for the softer ground (lower ground stiffness). The increased ground stiffness decreases the amplitude of the solar panel resonances and shifts the visible lander body-ground resonance peaks to higher frequency, as expected. The frequencies of these resonant modes in the seismic signal are unchanged by the propagation of the signal through the ground. Therefore, being able to identify the

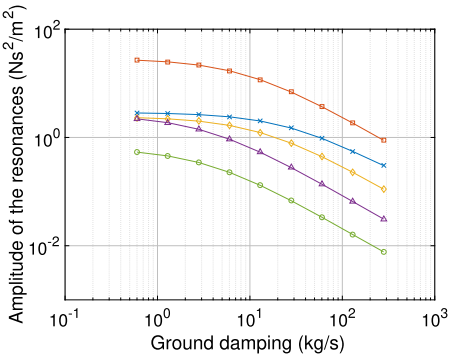


**Fig. 12** Variation of resonant frequency amplitudes with ground damping—each line corresponds to the peak frequency of five of the six different resonant modes (corresponding to the six degrees of freedom of the lander). The sixth resonant mode is not shown as its amplitude decreases too significantly with the increasing damping. Similarly, larger damping values are not shown as some of the resonant modes become entirely damped. The ground stiffness is maintained constant at the baseline value

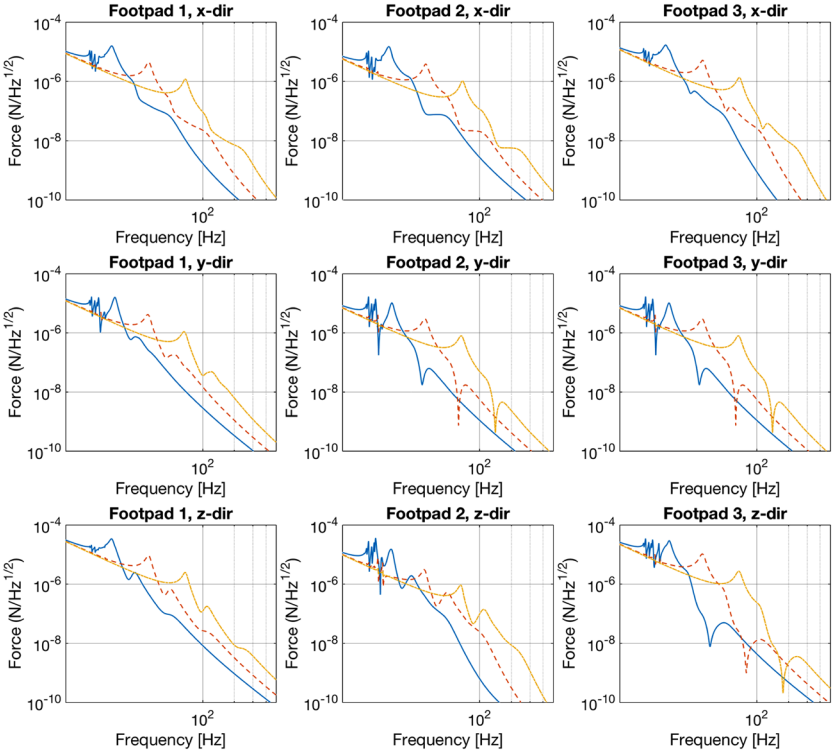


**Fig. 13** Influence of ground stiffness and damping on the force applied to the ground at the lander feet—the influence of both ground stiffness and ground damping on the resulting forces applied on the ground by each lander foot. Here the results of the baseline ground stiffness are shown (dashed red line) as are the results for a ground stiffness five times less than the baseline ground stiffness (solid blue line) and five times more than the baseline ground stiffness (dashed-dotted orange line). The ground damping parameter also varies, according to the relation in Eq. (10)

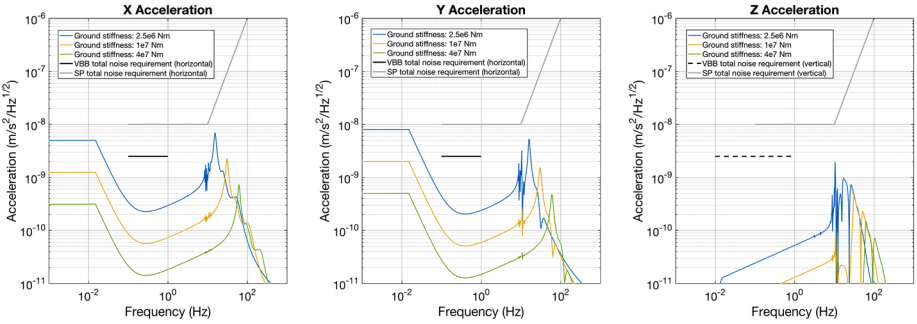


**Fig. 14** Influence of ground stiffness and damping on the resulting seismic signal—as the ground stiffness is influenced by the regolith density and both the P- and S-wave velocities, we chose here to modify the P- and S-wave velocities (two times less than the baseline values to two times more than the baseline values, the larger values being similar to the P- and S-wave velocities at ∼1 m depth or under the lander feet; Table 2) in order to produce different ground stiffnesses, while keeping the regolith density constant. The ground damping parameter also varies, according to the relation in Eq. (10)

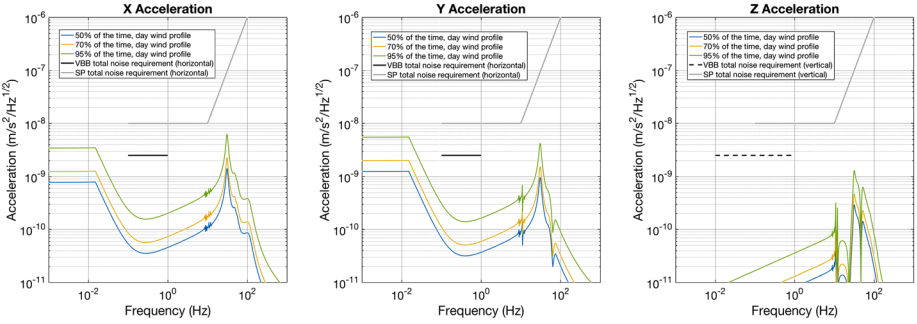


**Fig. 15** Influence of wind amplitude—the lander mechanical noise signal on SEIS in the (left) $x$-direction, (middle) $y$-direction, and (right) vertical direction, as calculated using the lander flexible mode model for the 50% wind day time profile (blue), the 70% wind day time profile (orange), and the 95% wind day time profile (green). The baseline parameters for this study, as presented in Sects. 3 and 2 were used except for the amplitude of the wind speed squared spectrum

resonance frequencies in the SEIS data will provide information on the regolith properties (Sect. 6.1).

## 5.2 Sensitivity to Wind Strength and Direction

The amplitude of the lander mechanical noise varies linearly with the amplitude of the wind speed squared spectrum. This is the case for the amplitudes of the resonant frequencies also. The frequencies of the resonances are not modified by the wind strength. This is demonstrated in Fig. 15 showing the lander mechanical noise signal for the three day-time spectral amplitudes (50%, 70% and 95% of the time; see Sect. 3.2 and Murdoch et al. 2017a), taking into account the flexible modes and using the baseline values for all parameters other than the wind spectral amplitude.

As the wind angle varies, the frequencies of the resonance modes remain unchanged. However, the relative amplitudes of the resonant modes vary as both the horizontal and vertical wind directions vary (Fig. 16). The amplitude changes with horizontal angle of

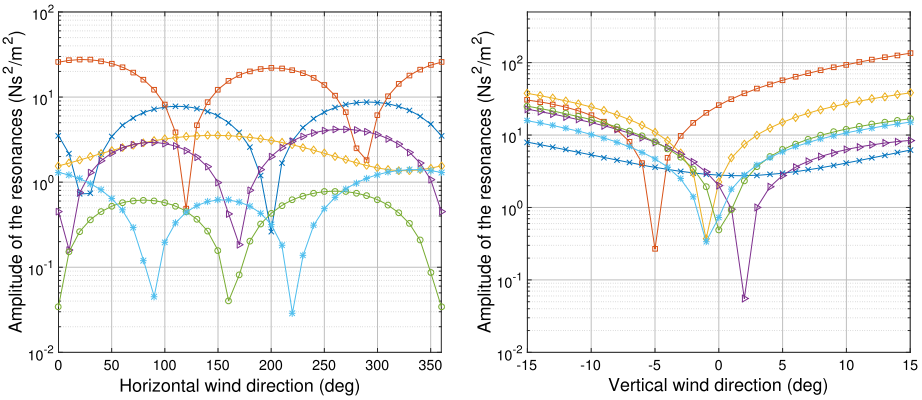


**Fig. 16** Variation of resonant frequency amplitudes with wind angle—(left) variation of resonant frequency amplitudes with horizontal wind angle. (Right) Variation of resonant frequency amplitudes with vertical wind angle. Each line corresponds to the peak frequency of the six different resonant modes. The amplitudes of the frequencies of the six resonant modes (corresponding to the six degrees of freedom of the lander) vary as the wind angle varies. The baseline parameters for this study, as presented in Sects. 3 and 2 were used except for the angle of attack of the wind on the lander

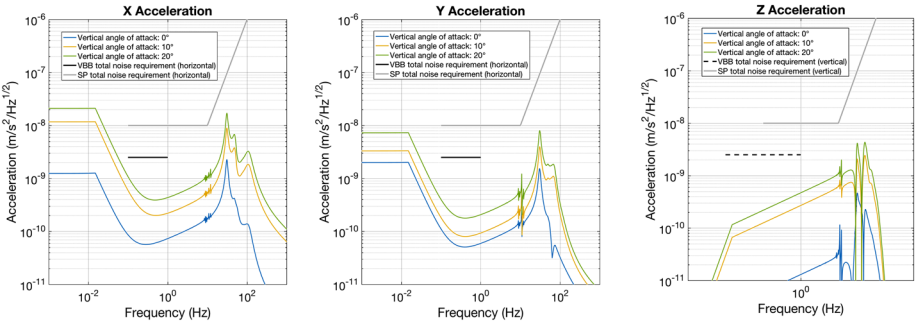


**Fig. 17** Influence of the vertical angle of attack on the resulting seismic signal—the resulting seismic signal on SEIS in the three axes as a function of the vertical angle of attack (0°—blue, 10°—orange, 20°—green). The baseline parameters for this study, as presented in Sects. 3 and 2 were used except for the vertical angle of attack of the wind. The total noise requirements for the seismic sensors are provided in black for the VBB sensors and grey for the SP sensors

attack are due to the varying direction of the force vector acting on the centre of pressure of the lander. The non-zero vertical angle of attack of the wind with respect to the lander body may occur when the wind flow is not laminar and parallel to the surface, if the lander is on locally sloped ground (the maximum expected lander inclination is 15°; Murdoch et al. 2017b), or if one or more of the feet are at slightly different heights from the others (for example, on a rock or in a small crater). The increasing amplitude of the resonance modes with the vertical wind direction corresponds to an increasing amplitude at all frequencies due to the larger lander lift and drag coefficients at larger vertical angles of attack (Fig. 4). The vertical angle of attack, therefore, has a large influence on the amplitude of the resulting seismic signal on SEIS, across the entire bandwidth of interest (Fig. 17).

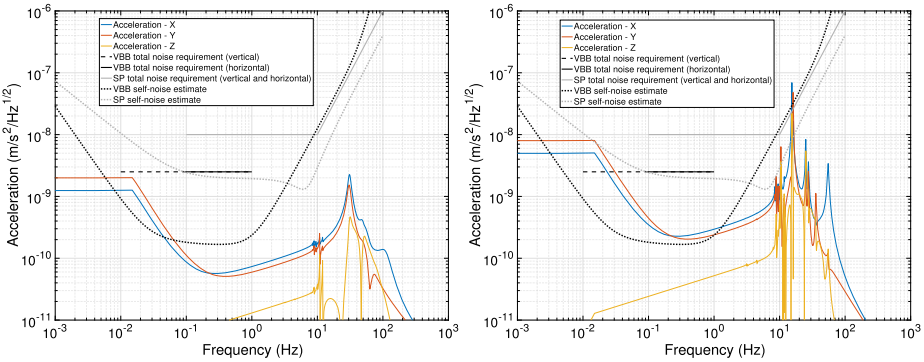


**Fig. 18** Comparison of the lander mechanical noise and the SEIS self noise—(left) the predicted lander mechanical noise using the baseline parameters for this study, as presented in Sects. 2 and 3. (Right) The predicted lander mechanical noise using the baseline parameters for this study, except for the ground parameters. Here the seismic velocities used are 50% of the baseline values, giving a ground stiffness of 2.5e6 N/m (rather than the baseline value of 9.9e6 N/m). We also assume that the coefficient in Eq. (10) is 0.01 rather than 0.1 giving a ground damping of ∼300 kg/s (rather than the baseline value of 6021 kg/s)

## 6 Implications for the Lander Mechanical Noise on Mars

For the baseline parameters chosen for this study, the mechanical noise on the SEIS instrument is not expected to exceed the instrument total noise requirements (Fig. 18, left). In fact, the self-noise of the sensors is expected to dominate the lander mechanical noise at all but the lowest frequencies in the horizontal axes, and the resonant frequencies are likely to be outside both the VBB and SP bandwidths. However, if the baseline parameter assumptions are not correct, the mechanical noise signal could become much more important. This is demonstrated for the case where all parameters are maintained constant except for the ground properties (Fig. 18, right). If the surface seismic velocities are reduced by 50% with respect to the baseline values (these velocities would be extremely low, but there are some examples of such low surface velocities from both the Moon and Earth e.g., Bachrach et al. 1998; Sutton and Duennebier 1970; Sollberger et al. 2016; Horvath et al. 1980; Mark and Sutton 1975), then the reduced ground stiffness reduces the frequency of the resonant modes thus bringing them into the SP bandwidth. A simultaneous reduction of the ground damping increases the amplitude of the resonances making some of them visible above the predicted self-noise of the SP sensors. Other factors such as a higher wind amplitude, an increased vertical angle of attack of the wind with respect to the lander, or a SEIS deployment position closer to the lander will also increase the amplitude of the lander mechanical noise compared with the noise estimated assuming the baseline parameters.

The azimuth of InSight after landing on Mars will be known and thus its position with respect to SEIS will be determined to within ±2 degrees. The correct azimuth can, therefore, be taken into account upon arrival to Mars. The tilt of both the lander and SEIS will also be known and can be accounted for. The continuous SEIS data will be nominally be acquired at 2 to 10 samples per second (Nyquist frequencies of 1 to 5 Hz). In this nominal mode, the resonant frequencies (generally >10 Hz) are unlikely to be observable in the seismic data and the mechanical noise contribution to the seismic signal will be limited to the lower frequency 'rigid' lander interactions. However, the seismic sensors can measure frequencies up to 50 Hz, depending on the operational mode in use. For such high sampling modes, the resonant frequencies may become an observable signal in the seismic data.

### 6.1 Determination of the Elastic Ground Properties of Mars

The elastic properties of the regolith have an important influence on the seismic wave-field and travel times as recorded by the SEIS instrument. Knowledge of the elastic properties of the regolith will help to better understand these effects which will need to be considered when analysing signals in the affected frequency range. In addition, the geotechnical properties of Martian regolith have implications for material strength, future robotic exploration of Mars, and the geological evolution of the InSight landing site.

The frequencies of the resonances associated with the lander body-ground interactions vary logarithmically with the ground stiffness (Fig. 11), but are unaffected by wind properties (amplitude or direction) and by the transmission through the ground to the seismometer. If the ground damping or the high frequency attenuation are too large, then the amplitudes of the resonances may not be sufficient to detect above the instrument self-noise. However, if it is possible to identify these resonances in the SEIS data, this should allow constraints to be placed on the elastic ground properties of the InSight landing site.

### 6.2 Determination of the Wind Properties on Mars

The mechanical noise of the lander may also provide an additional method for studying the wind properties on Mars. Measuring the shape of the wind spectrum on Mars across a large bandwidth, especially up to high frequencies ($>1$ Hz), would provide a unique opportunity to study the atmospheric turbulence on Mars (Spiga et al. 2018). As seen here and in Murdoch et al. (2017a), the shape of the mechanical noise closely follows that of the wind spectrum, giving direct access to wind spectrum shape. Such measurements would be complementary to the wind sensor on the InSight lander, and would provide data at higher frequencies: the wind sensor will be sampled at $\sim$1 Hz, matching its physical response time of roughly 1 second to wind perturbations (Spiga et al. 2018).

Our model predicts that the amplitude of the lander mechanical noise (including the resonant frequencies) should vary linearly with the amplitude of the wind speed squared spectrum. There is in agreement with the Viking Lander 2 mission measurements showing that the seismic amplitude measured by the seismometers on the lander deck was proportional to the square of the wind speed (Anderson et al. 1977; Nakamura and Anderson 1979; Lorenz 2012). Therefore, assuming that some knowledge is available about the wind direction (from the InSight wind sensors) and the ground properties at the landing site (either from studying the resonances, or from alternative techniques; Golombek et al. 2018), it may be possible to make some estimates of the wind amplitude. Such estimates could be then compared with those of the InSight wind sensor; the wind sensor accuracy is about $\pm 40\%$ for winds $<3.5\ \mathrm{m\,s^{-1}}$ (sensed to within about 1–1.5 $\mathrm{m\,s^{-1}}$), decreasing to $\pm 15\%$ for stronger winds (Spiga et al. 2018). Alternatively, using the wind speed estimates from the InSight wind sensors, the amplitudes of the resonant frequencies of the lander mechanical noise could be used to constrain the wind direction (Fig. 16).

## 7 Conclusions and Discussion

We have presented an updated model for estimating the lander mechanical noise on the InSight seismometer, SEIS, taking into account the flexible modes of the InSight lander. This new flexible mode model uses the Satellite Dynamics Toolbox (Alazard and Cumer 2014) to compute the direct and the inverse dynamic model of a satellite composed a main body fitted

with one or several dynamic appendages. For the InSight lander only cantilevered flexible appendages (the left and right solar panels) are considered, and each of these appendages is considered as a dynamic sub-structure

We then examine the seismic signal that will be produced on the InSight seismometers before studying in detail the sensitivity of our results to key environment parameters: the ground properties and the wind amplitude and direction. We find that the frequencies of the six dominant resonant modes (corresponding to the six degrees of freedom of the lander—ground interaction) increase logarithmically with increasing ground stiffness. However, the associated increase in the ground damping with increasing ground stiffness leads to a significant decrease in the amplitude of the resonances. The frequencies of the resonances are not modified by the wind strength or by the incoming wind angle. However, the amplitude of the lander mechanical noise (including the resonant frequencies) varies linearly with the amplitude of the wind speed squared spectrum, as observed during the Viking Lander 2 mission (Anderson et al. 1977; Nakamura and Anderson 1979; Lorenz 2012) and the relative amplitudes of the resonant modes vary as both the horizontal and vertical wind directions vary.

For the baseline parameters chosen for this study, the mechanical noise on the SEIS instrument is not expected to exceed the instrument total noise requirements (in agreement with the findings of Murdoch et al. 2017a). However, if the baseline parameter assumptions are found to be incorrect, the lander mechanical noise may be observable in the seismic data acquired by SEIS. In this case, the mechanical noise of the lander may also provide a method for studying the wind properties on Mars that would be complementary to the measurements of the InSight wind sensor. Similarly, if it is possible to identify the resonances in the SEIS data, this should allow constraints to be placed on the elastic ground properties of the InSight landing site.

The stresses exerted on the ground at the lander feet do not depend on the SEIS deployment position. However, the closer SEIS is to the lander, the larger the amplitude of the mechanical noise (as observed in Murdoch et al. 2017a). The static, elastic deformation hypothesis used to calculate the seismic signal on SEIS (Sect. 4) is a reasonable approximation in the [0.01–1] Hz bandwidth: given the seismic velocities in Table 2, typical wavelengths of seismic propagations are approximately 10 times or more larger than the typical distance between the lander feet and the SEIS feet. In this model the frequencies and relative amplitudes of the resonances do not change during the transmission of the forcing through the ground. However, at higher frequencies ($>10$ Hz), the lander-SEIS distance becomes comparable to the typical wavelengths of seismic propagations and the static deformation hypothesis may no longer be valid. Additionally, in real regolith, the behaviour is unlikely to be fully elastic and there will be some frequency dependant attenuation (Teanby et al. 2016; Myhill et al. 2018). As we have no frequency dependent attenuation in the elastic ground deformation model used, the amplitudes of the resonances in the observed seismic signal may be overestimated. However, although the amplitude of the seismic signal observed on SEIS may be influenced by these considerations, the frequencies of the resonances should not be modified. Therefore, if the resonant frequencies are observable in the SEIS data, it should still be possible to constrain the environment parameters such as the ground stiffness.

On the other hand, as mentioned in Sect. 2, the amplitudes of the solar panel resonances may be larger than predicted as the flexible mode model developed here does not take into account the direct action of the wind on the solar panels. Rather, it is assumed that the dynamic pressure acts on the centre of pressure of the lander body and the only force applied to the solar panels is the force applied by the main body at the appendage connection point. If the action of the wind on each solar panel could be taken into account, this may lead

to increased resonance amplitudes (particularly for the solar panel resonances at ~10 Hz). Currently, however, the information required about the InSight lander to develop a more accurate mechanical model is not readily available.

Finally, it should also be mentioned that the levelling structure of SEIS is expected to have resonant modes, and these are likely to be found at ~30 to 50 Hz depending on the ground properties (Fayon et al. 2018). However, as the lander resonances have both horizontal and vertical components, it should be possible to separate them from the levelling structure resonances that are expected to occur on the horizontal components only. The levelling structure resonances will also provide additional data to further constrain the physical properties of the upper regolith layer at the InSight landing site (Fayon et al. 2018).

**Acknowledgements** NAT and RM acknowledge support from the UK Space Agency. We acknowledge the following students from ISAE-SUPAERO who helped to prepare the flexible mode model: Alexandre Acerra-Gil, Aurelio de Aguiar-Rodrigues and Mouadh Bouayad. We would also like to thank an anonymous reviewer for their very constructive comments. This paper is InSight Contribution Number 61.

## References

D. Alazard and Ch. Cumer, Satellite Dynamics Toolbox: Principle, User Guide and tutorials (2014). https://personnel.isae-supaero.fr/daniel-alazard/matlab-packages/satellite-dynamics-toolbox.html

D.L. Anderson, W.F. Miller, G.V. Latham, Y. Nakamura, M.N. Toksoz, A.M. Dainty, F.K. Duennebier, A.R. Lazarewicz, R.L. Kovach, T.C.D. Knight, Seismology on Mars. J. Geophys. Res. **82**, 4524–4546 (1977). https://doi.org/10.1029/JS082i028p04524

R. Bachrach, J. Dvorkin, A. Nur, High-resolution shallow-seismic experiments in sand, part II: velocities in shallow unconsolidated sand. Geophysics **63**, 1234 (1998). https://doi.org/10.1190/1.1444424

M.J. Boussinesq, *Application des potentiels a l'étude de l'équilibre et du mouvement des solides élastiques* (Gauthier-Villars, Paris, 1885), p. 722.

J. Chebbi, V. Dubanchet, J.A.P. Gonzalez, D. Alazard, Linear dynamics of flexible multibody systems: a system-based approach. Multibody Syst. Dyn. **41**, 75–100 (2017). http://link.springer.com/journal/11044, http://oatao.univ-toulouse.fr/16559/

P. Delage, F. Karakostas, A. Dhemaied, M. Belmokhtar, P. Lognonne, M. Golombek, E.D. Laure, K. Hurst, J.-C. Dupla, S. Kedar, Y.J. Cui, W.B. Banerdt, An investigation of the mechanical properties of some Martian regolith simulants with respect to the surface properties at the InSight mission landing site. Space Sci. Rev. **211**, 191–213 (2017). https://doi.org/10.1007/s11214-017-0339-7

L. Fayon, B. Knapmeyer-Endrun, P. Lognonne, M. Bierwirth, et al., A numerical model of the SEIS Leveling system Transfer matrix and resonances: application to SEIS rotational seismology capability and SEIS dynamic ground interaction. Space Sci. Rev. (2018), submitted for publication

M. Golombek, M. Grott, G. Kargl, J. Andrade, et al., Geology and physical properties investigations by the InSight lander. Space Sci. Rev. **214**, 84 (2018)

J.A.P. Gonzalez, D. Alazard, T. Loquen, C. Pittet, C. Cumer, Flexible multibody system linear modeling for control using component modes synthesis and double-port approach. J. Dyn. Syst. Meas. Control **138**(12), 121004 (2016). http://oatao.univ-toulouse.fr/16566/

N. Guy, D. Alazard, C. Cumer, C. Charbonnel, Dynamic modeling and analysis of spacecraft with variable tilt of flexible appendages. J. Dyn. Syst. Meas. Control **136**(2), 021020 (2014). https://doi.org/10.1115/1.4025998.

P. Horvath, G.V. Latham, Y. Nakamura, H.J. Dorman, Lunar near-surface shear wave velocities at the Apollo landing sites as inferred from spectral amplitude ratios. J. Geophys. Res. **85**, 6572–6578 (1980). https://doi.org/10.1029/JB085iB11p06572

L.D. Landau, E.M. Lifshitz, *Theory of Elasticity*, 3rd edn. A Course of Theoretical Physics, vol. 7. (Pergamon, Elmsford, 1970)

P. Lognonné, T. Pike, in *Planetary Seismometry*, ed. by V.C.H. Tong, R.A. Garcia (Cambridge University Press, Cambridge, 2015)

P. Lognonné, J.G. Beyneix, W.B. Banerdt, S. Cacho, J.F. Karczewski, M. Morand, Ultra broad band seismology on InterMarsNet. Planet. Space Sci. **44**(11), 1237–1249 (1996). https://doi.org/10.1016/S0032-0633(96)00083-9. http://www.sciencedirect.com/science/article/pii/S0032063396000839

R.D. Lorenz, Planetary seismology—expectations for lander and wind noise with application to Venus. Planet. Space Sci. **62**, 86–96 (2012). https://doi.org/10.1016/j.pss.2011.12.010

N. Mark, G.H. Sutton, Lunar shear velocity structure at Apollo sites 12, 14, and 15. J. Geophys. Res. **80**, 4932–4938 (1975). https://doi.org/10.1029/JB080i035p04932

E. Millour, F. Forget, A. Spiga, T. Navarro, J.-B. Madeleine, L. Montabone, A. Pottier, F. Lefevre, F. Montmessin, J.-Y. Chaufray, M.A. Lopez-Valverde, F. Gonzalez-Galindo, S.R. Lewis, P.L. Read, J.-P. Huot, M.-C. Desjean, MCD/GCM development Team, The Mars climate database (MCD version 5.2), in *European Planetary Science Congress 2015*, 27 September–2 October, 2015, Nantes, France, vol. 10 (2015). EPSC2015-438. http://meetingorganizer.copernicus.org/EPSC2015

D. Mimoun, N. Murdoch, P. Lognonné, K. Hurst, W.T. Pike, J. Hurley, T. Nébut, W.B. Banerdt, S. Team, The noise model of the SEIS seismometer of the InSight mission to Mars. Space Sci. Rev. (2017). https://doi.org/10.1007/s11214-017-0409-x

P. Morgan, M. Grott, G. M., P. Delage, B. Knapmeyer-Endrun, A pre-landing assessment of regolith properties at the InSight landing site. Space Sci. Rev. **214**, 104 (2018)

N. Murdoch, D. Mimoun, R.F. Garcia, W. Rapin, T. Kawamura, P. Lognonné, Evaluating the wind-induced mechanical noise on the InSight seismometers. Space Sci. Rev. (2017a). https://doi.org/10.1007/s11214-016-0311-y

N. Murdoch, B. Kenda, T. Kawamura, A. Spiga, P. Lognonné, D. Mimoun, W.B. Banerdt, Estimations of the seismic pressure noise on Mars determined from large eddy simulations and demonstration of pressure decorrelation techniques for the InSight mission. Space Sci. Rev. (2017b). https://doi.org/10.1007/s11214-017-0343-y

R. Myhill, J. Teanby, N. Wookey, N. Murdoch, Frequency dependence of seismic attenuation and coupling through Mars' regolith: implications for the InSight Mission. Space Sci. Rev. (2018). https://doi.org/10.1007/s11214-018-0514-5

Y. Nakamura, D.L. Anderson, Martian wind activity detected by a seismometer at Viking lander 2 site. Geophys. Res. Lett. **6**, 499–502 (1979). https://doi.org/10.1029/GL006i006p00499

Y. Nishikawa, A. Araya, K. Kurita, N. Kobayashi, T. Kawamura, Designing a torque-less wind shield for broadband observation of marsquakes. Planet. Space Sci. **104**, 288–294 (2014). https://doi.org/10.1016/j.pss.2014.10.011

D. Sollberger, C. Schmelzbach, J.O.A. Robertsson, S.A. Greenhalgh, Y. Nakamura, A. Khan, The shallow elastic structure of the lunar crust: new insights from seismic wavefield gradient analysis. Geophys. Res. Lett. **43**, 10 (2016). https://doi.org/10.1002/2016GL070883

A. Spiga, N.A. Teanby, F. Forget, A. Lucas, D. Banfield, et al., Atmospheric science with InSight. Space Sci. Rev. **214**, 109 (2018)

T. Spohn, M. Grott, S. Smrekar, C. Krause, T.L. Hudson, HP3 Instrument Team, Measuring the Martian heat flow using the heat flow and physical properties package (HP3), in *Lunar and Planetary Science Conference*. Lunar and Planetary Science Conference, vol. 45 (2014), p. 1916

G.H. Sutton, F.K. Duennebier, Elastic properties of the lunar surface from surveyor spacecraft data. J. Geophys. Res. **75**, 7439–7444 (1970). https://doi.org/10.1029/JB075i035p07439

N.A. Teanby, J. Stevanovic, J. Wookey, N. Murdoch, J. Hurley, R. Myhill, N.E. Bowles, S.B. Calcut, W.T. Pike, Anelastic seismic coupling of wind noise through Mars' regolith for NASA's InSight Lander at short periods. Space Sci. Rev. (2016). https://doi.org/10.1007/s11214-016-0310-z